An Ovol2-Zeb1 transcriptional circuit regulates epithelial directional migration and proliferation

Daniel Haensel[1], Peng Sun[1], Adam L MacLean[2], Xianghui Ma[1], Yuan Zhou[1], Marc P Stemmler[3], Simone Brabletz[3], Geert Berx[4,5], Maksim V Plikus[6], Qing Nie[2,6], Thomas Brabletz[3] & Xing Dai[1,*] (iD)

Abstract

Directional migration is inherently important for epithelial tissue regeneration and repair, but how it is precisely controlled and coordinated with cell proliferation is unclear. Here, we report that Ovol2, a transcriptional repressor that inhibits epithelial-to-mesenchymal transition (EMT), plays a crucial role in adult skin epithelial regeneration and repair. *Ovol2*-deficient mice show compromised wound healing characterized by aberrant epidermal cell migration and proliferation, as well as delayed anagen progression characterized by defects in hair follicle matrix cell proliferation and subsequent differentiation. Epidermal keratinocytes and bulge hair follicle stem cells (Bu-HFSCs) lacking Ovol2 fail to expand in culture and display molecular alterations consistent with enhanced EMT and reduced proliferation. Live imaging of wound explants and Bu-HFSCs reveals increased migration speed but reduced directionality, and post-mitotic cell cycle arrest. Remarkably, simultaneous deletion of *Zeb1* encoding an EMT-promoting factor restores directional migration to *Ovol2*-deficient Bu-HFSCs. Taken together, our findings highlight the important function of an Ovol2-Zeb1 EMT-regulatory circuit in controlling the directional migration of epithelial stem and progenitor cells to facilitate adult skin epithelial regeneration and repair.

Introduction

Directional migration of epithelial cells is an integral component of tissue development, regeneration, and repair [1–3]. While the cellular and molecular machineries responsible for cell movements are relatively well delineated, little is known about the transcriptional mechanisms that regulate gene expression in epithelial stem and progenitor cells to ensure their directional and collective migration for efficient regeneration and repair. Moreover, how migration of epithelial stem and progenitor cells is coordinated with their proliferative activity during tissue expansion is unclear.

Mouse skin serves as a leading model to study the molecular and cellular mechanisms that control epithelial stem cell function and tissue regeneration [4]. During homeostasis, skin epidermis is maintained by epithelial stem cells in the innermost basal layer, which can either self-renew, or follow an upward path to differentiate into spinous and granular cells of the suprabasal layers culminating in the formation of a protective outer permeability barrier [4]. Upon skin injury and integral to the healing process, epidermal cells at the wound margin become activated to re-epithelialize the wound [5,6]. Central to re-epithelialization are the collective migration of epidermal basal/spinous cells immediately adjacent the wound and the proliferation of basal cells further out on the wound periphery [7]. Migrating keratinocytes exhibit molecular, morphological, cytoskeletal, and adhesive changes that bear resemblance to those occurring during epithelial-to-mesenchymal transition (EMT) [8], leading to the prevailing notion that wound re-epithelialization is a partial EMT process [9]. However, to date, the precise role of EMT-regulatory proteins in epidermal cell migration during wound healing remains to be elucidated.

Adult hair follicles (HFs) undergo cycles of regression (catagen), resting (telogen), and growth (anagen) [10]. Regeneration of a new HF is fueled by stem cells that reside in the bulge (Bu-HFSCs) and their early progenies in the secondary hair germ (HG) [4,11]. During telogen-to-anagen transition, HG cells and Bu-HFSCs become sequentially activated, unleashing a coordinated program of active proliferation and differentiation to generate multiple cell types constituting the new HF [12]. Tantalizing clues implicate the pro-migratory nature of Bu-HFSCs and their progenies in the HG and outer root sheath. Live cell imaging and lineage tracing have detected Bu-HFSC migration within and out of the niche [13,14].

1 Department of Biological Chemistry, School of Medicine, University of California, Irvine, CA, USA
2 Department of Mathematics, University of California, Irvine, CA, USA
3 Department of Experimental Medicine, Nikolaus-Fiebiger-Center for Molecular Medicine, Friedrich-Alexander University Erlangen-Nuernberg, Erlangen, Germany
4 Molecular and Cellular Oncology Lab, Department of Biomedical Molecular Biology, Ghent University, Zwijnaarde, Belgium
5 Cancer Research Institute Ghent (CRIG), Ghent, Belgium
6 Department of Developmental and Cell Biology, University of California, Irvine, CA, USA
*Corresponding author. Tel: +1 949 824 3101; Fax: +1 949 824 2688; E-mail: xdai@uci.edu

During wound healing, Bu-HFSCs cells also travel toward the skin surface to transiently participate in repair of the interfollicular epidermis (IFE) [15,16]. HG cells also undergo dynamic movements to support the downward extension of the new HF, and contain a keratin 79-positive subset that becomes specified during early anagen and migrates upwards to initiate hair canal formation [13,17]. Furthermore, outer root sheath cells of the lower HF are capable of rapid and long-range migration during anagen progression [13,18]. It has been reported that Bu-HFSC-specific transcription factor (TF) Sox9 activates other Bu-HFSC-TFs when ectopically expressed in epidermal keratinocytes [19] and confers enhanced invasive migration [20]. However, at present very little is known about the transcriptional mechanisms that regulate Bu-HFSC migration and the importance of such control mechanisms in HF regeneration.

Ovol2, a member of the Ovo family of zinc finger TFs, has recently been identified as a critical EMT-inhibitory factor in developing skin and mammary epithelia [21,22]. These studies prompted us to ask whether Ovol2 also regulates epidermal repair and HF regeneration in adult skin, and if yes whether this role is mechanistically linked to the control of cell migration. We show that epithelia-specific loss of Ovol2 results in aberrant wound re-epithelialization, delayed anagen progression, and compromised HF regeneration. We provide *ex vivo* and *in vivo* evidence that *Ovol2*-deficient epidermal cells and Bu-HFSCs migrate faster than their control counterparts, but with reduced directionality and proliferation. The migratory defects are near-completely rescued by simultaneous deletion of *Zeb1*, which encodes an EMT-inducing TF [23]. Together, our findings highlight an important role for EMT-regulatory factors in fine-tuning the migration and proliferation of skin epithelial stem cells to facilitate optimal tissue regeneration and repair.

Results

Ovol2-deficient newborn keratinocytes show compromised colony formation, and altered expression of EMT and cell cycle genes

To probe a functional requirement for *Ovol2* in skin, we first examined the *in vitro* behavior of newborn primary keratinocytes (NBPKs) derived from skin epithelia-specific *Ovol2* knockout (*Ovol2* SSKO: *K14-Cre*; *Ovol2*$^{f/-}$) mice. Despite lack of a remarkable embryonic epidermal phenotype *in vivo* [21], compared with control counterparts, *Ovol2*-deficient NBPKs grew slower at a high density (Fig 1A) and formed fewer colonies at a clonal density (Fig 1B). Closer examination of individual colonies over time revealed that *Ovol2* SSKO cells were capable of initial attachment and divisions, but failed to continuously expand and/or to maintain proper intercellular adhesion (Figs 1B and C, and EV1A and B).

To seek molecular insights, RNA sequencing (RNA-seq) was performed to examine global gene expression differences between control and *Ovol2* SSKO NBPKs. This analysis revealed 748 significantly upregulated and 740 significantly downregulated genes (greater than 2-fold difference, $P < 0.05$) in *Ovol2*-deficient cells (Figs 1D and EV1C; for a complete list of the differentially expressed genes, see Dataset EV1). Gene Ontology (GO) analysis of the differentially expressed genes revealed EMT genes to be the most highly enriched, and cell cycle genes to be the most reduced, in

Ovol2 SSKO NBPKs (Fig 1E). Gene Set Enrichment Analysis (GSEA) confirmed enrichment or de-enrichment of these GO-identified gene signatures (Figs 1F and EV1D and E). Furthermore, the upregulated expression of select EMT genes, *Zeb1* and *Vim*, as well as the downregulated expression of select cell cycle genes, *Ki67* and *Cdk1,* was validated by RT–qPCR (Fig 1G). Together, these data uncover reduced proliferative expansion and increased EMT tendency as two major defects of *Ovol2*-deficient epidermal cells in culture.

Ovol2 is expressed in the proliferative compartments of adult skin epithelia during homeostasis and repair

Toward examining the *in vivo* function of Ovol2, we determined its expression in adult skin. Indirect immunofluorescence revealed the presence of nuclear Ovol2 protein in IFE basal and some suprabasal cells (Fig 2A). In HFs, nuclear Ovol2 was detected at telogen in cells within the bulge and HG, and at early anagen in the presumptive matrix with the highest expression in cells directly abutting dermal papilla (DP; Fig 2B and C). During excisional wound healing, nuclear Ovol2 protein was abundant in epidermal cells of the highly proliferative zone just outside the wound margin, but completely absent in the migrating front that is known to be devoid of active proliferation [7] (Fig 2D–I). Mixed nuclear (predominantly in suprabasal cells) and cytoplasmic (predominantly in basal cells) signals were detected in the intermediate regions (Fig 2F–H), which is curious and may implicate the possibility of previously undocumented nuclear-cytoplasmic shuttling of Ovol2, a notion that is outside the scope of this work. Consistent with regional protein distribution, *Ovol2* mRNA expression was higher in the wound proliferative zone than the leading edge [7] (Fig 2J). Overall, these data show that Ovol2 protein is present in stem and progenitor cells of the IFE and HF, with expression seemingly correlating with a more proliferative but less migratory cellular state.

Ovol2 is required for efficient wound repair and promotes directional migration of wound epidermal cells

To investigate the role of Ovol2 in epidermal wound repair, we turned to an excisional wound splinting model [24] to minimize myofibroblast-driven contraction and to enable measuring wound closure as a direct consequence of re-epithelialization (Fig EV2A). Compared to littermate controls, *Ovol2* SSKO mice showed delayed wound closure during a 7-day period. By post-wounding day (PWD) 7, *Ovol2* SSKO and control wounds were 30 and 15%, respectively, of the original wound area (Figs 3A and EV2B). Interestingly, at the histological level on PWD 3, the migrating front in *Ovol2* SSKO wounds had a significantly longer contour and showed apparently abnormal cellular adhesions compared to control counterparts (Fig 3B and C). When epidermal cells were genetically marked (mediated by *K14-Cre*) for β-galactosidase (β-gal) or GFP reporter expression to better visualize the neo-epidermis, it became obvious that the leading edges in *Ovol2* SSKO mice had multiple spikes, rough edges, branches, and grooves (Figs 3C and EV2C). Moreover, some *Ovol2*-deficient epidermal cells appeared to have disseminated away from the main body of the leading edges (Fig 3C).

Next, we compared cell proliferation in control and *Ovol2* SSKO wounds. Consistent with previous reports [7,25], epidermal cells
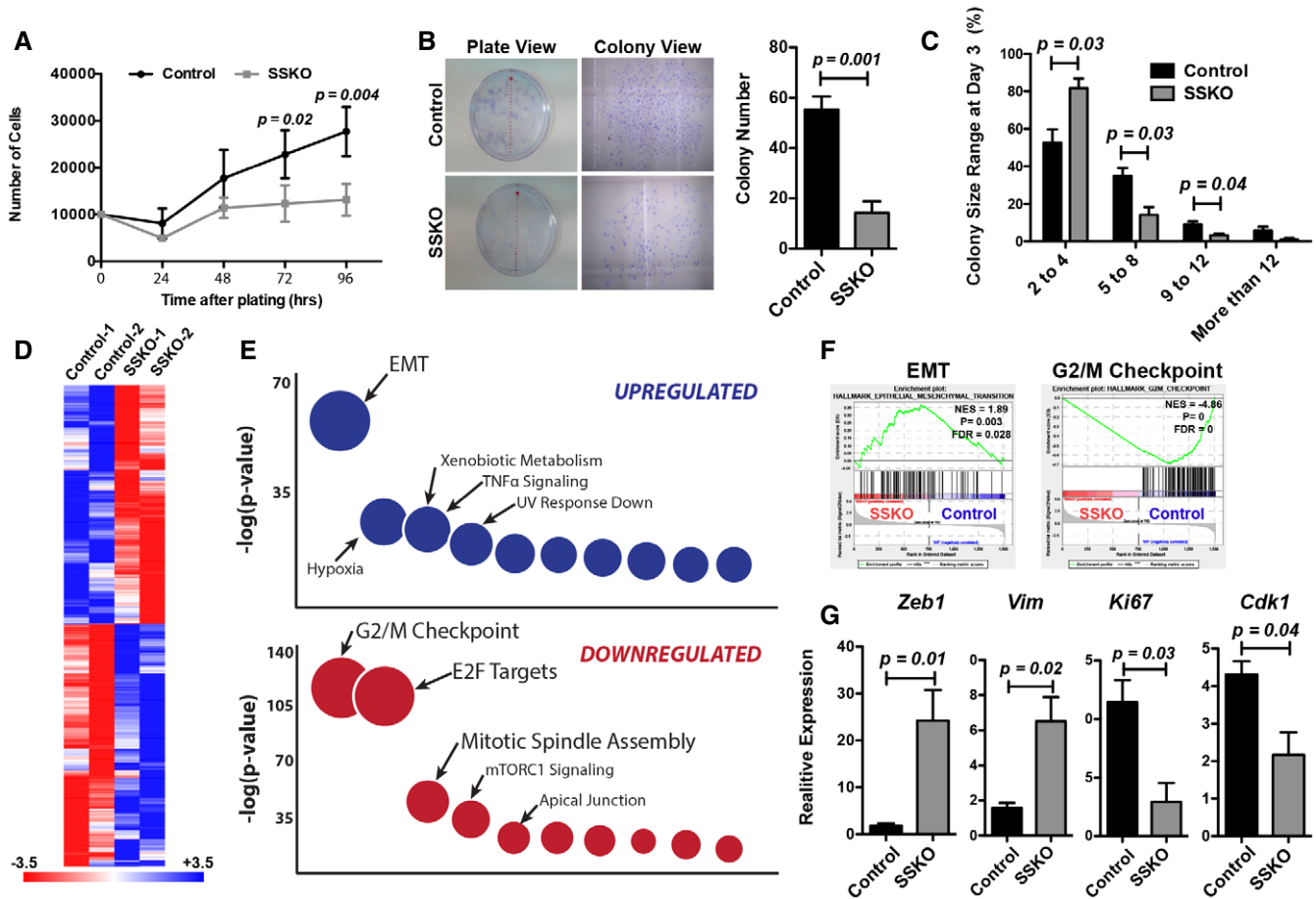
Figure 1. Growth and gene expression defects in *Ovol2*-deficient NBPKs.

A   Growth curve of cells cultured at high densities (*n* = 3 pairs).

B   Results of clonal assays at 14 days after plating. Representative images are shown on the left, and quantification of multiple assays on the right (*n* = 3 pairs).

C   Distribution of colony size (i.e., number of cells per colony) at 3 days after plating (*n* = 3 pairs).

D   Heat map of genes differentially expressed (*P* < 0.05) in control and *Ovol2* SSKO NBPKs. Plotted values are $\log_{10}$(FPKM).

E   GO analysis of the top up- or downregulated gene sets.

F   GSEA analysis of RNA-seq data. NES, normalized enrichment score. FDR, false discovery rate.

G   RT–qPCR of the indicated genes normalized to *Gapdh* (*n* = 3 pairs).

Data information: For statistical analysis in (A), (B), (C), and (G), we used an unpaired two-tailed Student's *t*-test. Error bars in (A), (B), (C), and (G) represent mean ± SEM.

distal to the wound in control mice at PWD 3 exhibited a higher proliferative activity than epidermal cells proximal to the wound (Fig 3D). Compared to control mice, significantly reduced numbers of Ki67-positive cells were observed in both wound-distal and wound-proximal regions of the *Ovol2* SSKO mice (Fig 3D and E).

Wound explant outgrowth is an established method to measure *ex vivo* wound epidermal cell migration [26]. Analysis of explant cultures of control and *Ovol2* SSKO wounds revealed decreased overall outgrowth in the latter (Fig 3F and G). Live cell imaging analysis shows that even though individual cells from *Ovol2*-deficient explants migrated greater distances within a given time period (18 h), their directionality was reduced as compared to the controls (Fig 3H–J, Movies EV1 and EV2). When the full step length and straightness distributions of the migrating cells were plotted, it was clear that *Ovol2*-deficient keratinocytes took larger and more variable steps (Fig 3K), but with less straight paths (Fig 3L). Examination of the distribution of turning angles between steps corroborated

the loss of persistence of *Ovol2*-deficient cells (much lower density near 0 than for control cells; Fig EV2D). Decreased proliferation and aberrant migration of epidermal cells thus underlie the wound healing defect in *Ovol2* SSKO mice.

Loss of *Ovol2* compromises HF regeneration and Bu-HFSC expansion

Data in the preceding sections demonstrate a functional involvement of *Ovol2* in regulating IFE cell proliferation, adhesion, and migration under culturing and wound healing conditions. Previously, we reported that Ovol2 overexpression results in hair loss and HF defects characterized by precocious telogen-to-anagen progression [21], prompting us to examine a physiological role of Ovol2 in HF regeneration during adult hair cycle. Indeed, a mild but reproducible delay in the progression of the first postnatal anagen was observed in *Ovol2* SSKO mice (Figs 4A–C and EV3A). Although
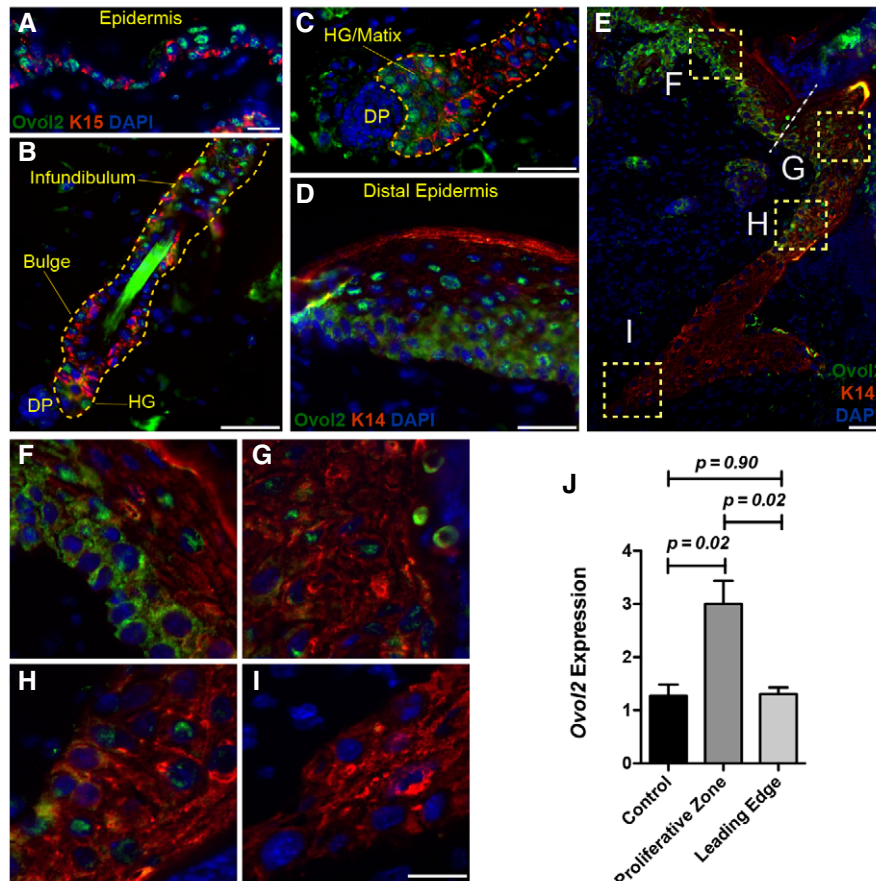
Figure 2. Ovol2 expression in normal (A–C) and wounded (D–I) adult skin.

A–I   Ovol2 protein expression revealed by indirect immunofluorescence. Enlarged images of the boxed areas in (E) are shown as (F–I) to indicate Ovol2 protein distribution in the intermediate regions (F–H) between the proliferative zone (D) and the migrating front (I). White dashed line in (E) indicates the wound margin. DAPI stains the nuclei.

J   RT–qPCR analysis of unwounded skin (control) and microdissected wound regions (n = 3 mice).

Data information: Scale bar, 50 μm in (A–D and F–I); 100 μm in (E). For statistical analysis in (J), we used an unpaired two-tailed Student's t-test. Error bars in (J) represent mean ± SEM.

Ki67-positive HG cells were observed in *Ovol2* SSKO mice at P22, the presumptive matrix structures were less developed in the new mutant HFs than control counterparts (Fig 4D). Moreover, anagen HFs were generally less elongated in *Ovol2* SSKO skin, their bulbs were smaller, and their differentiated lineages were poorly represented compared to control counterparts (Figs 4A–C and EV3B and C). Even in residual mutant HFs with lengths comparable to control HFs, hair keratin expression was reduced as revealed by AE13 antibody staining (Fig 4E). It appears as if the outer root sheath cells are migrating downwards to extend the HF, but the matrix cells are not efficiently dividing and migrating upwards to produce the differentiated progenies. Despite these defects, HFs in *Ovol2* SSKO mice were able to reach second telogen by P49 just as in the WT (Fig 4A) and were able to produce new hair shafts (Fig EV3D). There was no hair loss phenotype, and the epidermal thickness was not affected throughout these stages examined (Fig EV3E). Taken together, our data demonstrate a functional requirement for *Ovol2* in the timely downgrowth of, and subsequent differentiation within, postnatal HFs.

Next, we asked if Bu-HFSCs are affected by *Ovol2* loss. The percentage of CD49f^{Hi}CD34$^+$ Bu-HFSCs of total epithelial cells (CD49f$^+$) was similar between control and *Ovol2* SSKO mice at P23, but was significantly reduced at P49 (Fig EV3F and G) [27]. However, even at P23, gene expression differences were already evident, as freshly sorted SSKO Bu-HFSCs exhibited upregulated (more than 10-fold) expression of *Zeb1* but downregulated expression of *Ki67* and *Cdk1* compared to controls (Fig 4F). Subsequent functional characterizations focused on Bu-HFSCs isolated at P49, when control and SSKO HFs were both in telogen. When plated in culture at a clonal density, control Bu-HFSCs were able to produce colonies that continuously expanded over a period of 2 weeks. In sharp contrast, *Ovol2*-deficient Bu-HFSCs, while able to form small colonies initially, failed to sustain clonal growth leading to dramatically reduced number and size of the colonies at the end of culture (Figs 4G–I and EV4A). Furthermore, the few mutant colonies that reached large sizes exhibited abnormal morphology with enlarged intercellular gaps, increased levels of *Zeb1* and *Vim* mRNAs but reduced level of *Cdk1* mRNA, and a higher frequency of nuclear
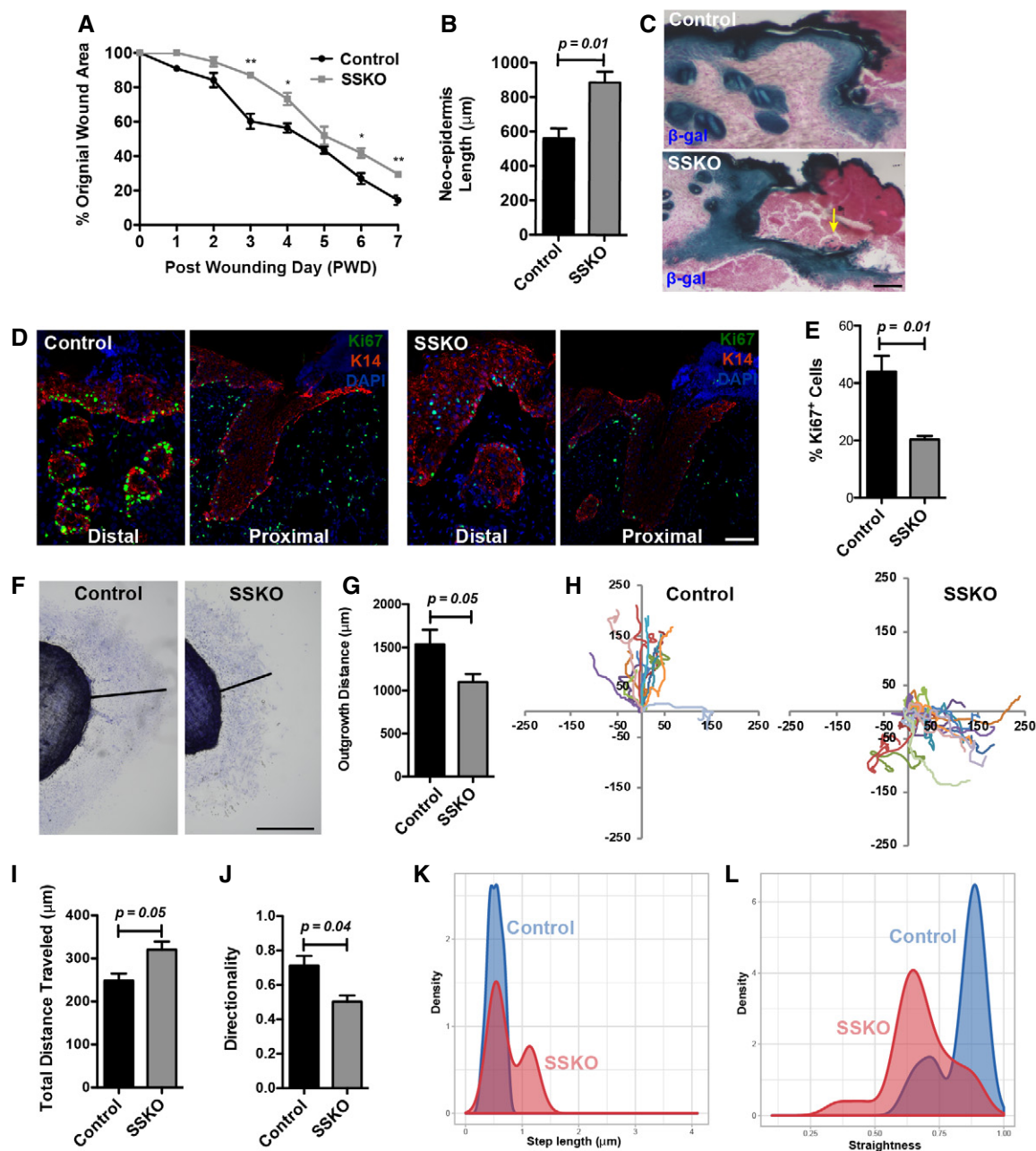
Figure 3. *In vivo* and *ex vivo* evidence for skin wound healing defects in *Ovol2* SSKO mice.

A   Percent of original wound area over 7 days after wounding (*n* = 3 pairs; *P < 0.05; **P < 0.005).

B   Length of the neo-epidermis (outer contour of the migrating front up to the wound margin) at PWD 3 (*n* = 3 pairs).

C   Morphology of the leading edges in control (*Ovol2^{fl/+};K14-Cre;ROSA26R*) and *Ovol2* SSKO (*Ovol2^{fl/−};K14-Cre;ROSA26R*) wounds. Yellow arrow points to disseminating cells.

D, E   Proliferation analysis by Ki67 immunostaining. Percent Ki67$^+$ cells (E) were calculated as the number of Ki67$^+$ cells within the neo-epidermis over the total number of DAPI-stained nuclei (*n* = 3 pairs).

F   Representative wound explants stained with crystal violet.

G   Quantification of the outgrowth distance of multiple explants from (F) (*n* = 3 pairs).

H   Movement tracks of individual cells in control and *Ovol2* SSKO explants over 18 h of live imaging.

I–L   Quantitative analysis of total distance traveled (I), directionality (J), full step length (K), and straightness distribution (L) of multiple cells in control and SSKO explants (*n* = 3 pairs).

Data information: Scale bar, 100 μm in (C) and (D), 1,000 μm in (F). For statistical analysis in (A), (B), (E), (G), (I), and (J), we used an unpaired two-tailed Student's *t*-test. For statistical analysis in (K) and (L), we used Kolmogorov–Smirnov test with *P* = 0.005 and *P* = 0.0001, respectively. Error bars in (A), (B), (E), (G), (I), and (J) represent mean ± SEM.
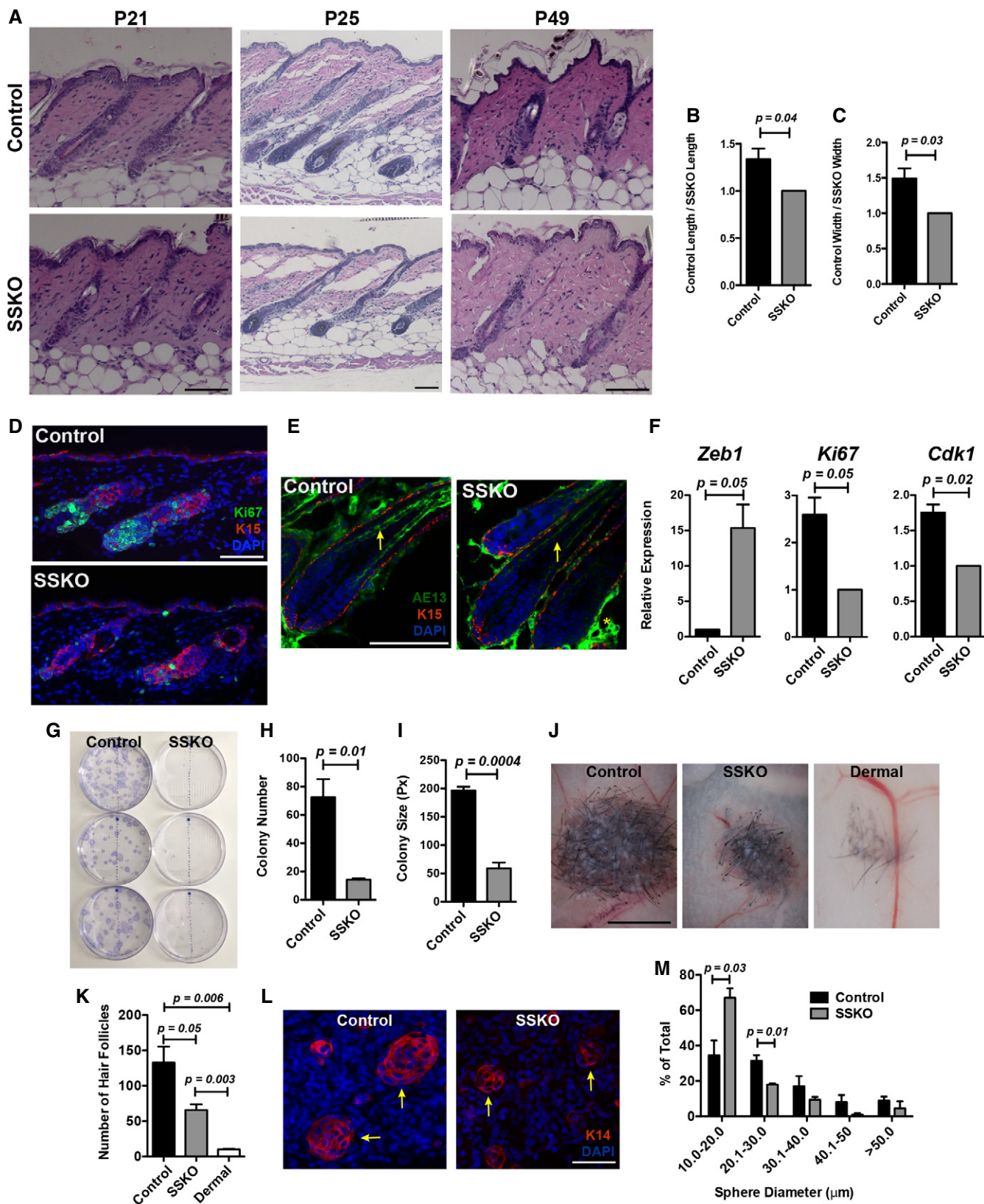
Figure 4.

◄

Figure 4. *In vivo* and *ex vivo* evidence for *Ovol2* loss-induced HF defects.

A   H/E analysis of control and *Ovol2* SSKO skin at the indicated ages.
B, C   Fold difference in HF length (B) and bulb width (C) between control and *Ovol2* SSKO mice at the ages of P22–P26 (*n* = 5 pairs).
D   Ki67 immunostaining in control and *Ovol2* SSKO skin. K15 stains the bulge/HG cells.
E   AE13 immunostaining. Arrows and "*" indicate specific and background signals, respectively.
F   RNA expression of the indicated genes normalized to *Gapdh* in freshly sorted P23-Bu-HFSCs (*n* = 3 pairs).
G   Clonal analysis of control and *Ovol2* SSKO Bu-HFSCs.
H, I   Number (H) and average size (I) of Bu-HFSC colonies from (G) (*n* = 3 pairs).
J   Representative images of patch assay results using control and *Ovol2* SSKO epidermal cells along with dermal-only control.
K   Quantification of number of HFs (*n* = 3 pairs; each biological replicate is an average of three injections).
L   K14 immunostaining of skin from the injection site at 3 days after injection. Arrow points to epidermal spheres.
M   Quantification of epidermal sphere diameter (three independent experiments using three pairs of control and *Ovol2* SSKO mice) at 3 days after injection.

Data information: Scale bar, 50 μm in (A), (D), (E), and (L), 250 μm in (J). For statistical analysis in (B), (C), (H), (I), (K), and (M), we used an unpaired two-tailed Student's *t*-test. For statistical analysis in (F), we used a paired two-tailed Student's *t*-test. Error bars in (B), (C), (F), (H), (I), (K), and (M) represent mean ± SEM.

Zeb1-positive cells (Fig EV4B–E). Collectively, these data show that *Ovol2* is required for maintaining the epithelial state and active expansion of Bu-HFSCs.

To investigate the *in vivo* consequence of defective clonal adhesion and expansion of *Ovol2*-deficient cells, we turned to "patch" assay, a well-established transplantation model to examine the hair/HF regenerative capacity of isolated skin epithelial cells [28]. Control or *Ovol2* SSKO epidermal cells in single-cell suspension were combined with wild-type newborn dermal cells and subcutaneously injected into the backs of *Nu/J* mice. Two weeks later, significantly fewer hairs/HFs were observed in patches derived from *Ovol2* SSKO epidermal cells than the littermate control cells (Fig 4J and K). Interestingly, at earlier time points when injected epidermal cells first aggregated and began to proliferate [28], the K14⁺ spheres formed by *Ovol2* SSKO cells were significantly smaller than those formed by control cells (Fig 4L and M). These data demonstrate that in the absence of *Ovol2*, adult epidermal cells have a reduced capacity to regenerate HFs, which appears to stem from early defects in epithelial sphere formation.

Live cell imaging reveals an intimate link between aberrant migration and defective cell cycle progression of *Ovol2*-deficient Bu-HFSCs

To probe the potential mechanism of *Ovol2* deficiency-induced Bu-HFSC clonal expansion defects, we utilized live cell imaging to track individual colonies over time. Freshly sorted control Bu-HFSCs generated colonies after 7 days in culture and cells within these colonies exhibited a remarkably rapid doubling rate leading to a > 2-fold increase in cell number over an 18-h period, whereas the doubling rate of *Ovol2* SSKO cells was significantly lower (Fig 5A, Movies EV3 and EV4). More than 80% of the dividing cells in control colonies rounded up slightly and transiently when undergoing mitosis—a phenomenon previously identified as mitotic cell rounding [29], but they quickly reattached *in situ* after generating two daughter cells (Fig 5B and C; type-1 division). Less than 20% of the dividing cells, particularly those that reside in the periphery of the colonies, rose up significantly above the plane of the neighboring cells (Fig 5B and C; type-2 division). In stark contrast, the relative numbers of rounded-up cells and type-2 divisions were significantly higher for *Ovol2*-deficient cells (Figs 5B and C, and EV4A). Furthermore, these dividing mutant cells often migrated away from their original positions, failed to reattach, and the two

daughter cell nuclei remained connected after an extensive period of time (Fig 5C).

The prolonged connection of daughter cell nuclei in *Ovol2*-deficient colonies led us to wonder whether without *Ovol2* cell cycle is arrested post-mitosis. Indeed, flow cytometry-mediated cell cycle analysis of actively growing Bu-HFSCs revealed a significantly increased number of G2/M cells accompanied by a decreased number of G1 cells in *Ovol2* SSKO culture, whereas the percent of S-phase cells was unaffected (Fig 5D). As expected [12], flow cytometric analysis of freshly isolated Bu-HFSCs from telogen back skin revealed few cycling (G2/M/S phase) cells, and no difference was detected between control and *Ovol2*-deficient cells (Fig EV4F). These data suggest that during active expansion, *Ovol2*-deficient Bu-HFSCs cannot efficiently transition from G2/M to G1 phase of the cell cycle.

Ovol2 promotes directional migration of Bu-HFSCs through suppressing *Zeb1* expression

The ability to track Bu-HFSC colonies over time enabled us to monitor the migratory behavior of single cells as colonies are expanding. While control Bu-HFSCs migrated outwards with relatively straight trajectories, *Ovol2* SSKO cells followed less straight/persistent paths (Fig 6A, Movies EV3 and EV4). On average, mutant cells migrated greater overall distances with greater velocities than control cells, but the directionality of migration was severely compromised (Fig 6B). Moreover, *Ovol2*-deficient cells took larger and more variable steps (Fig 6C), moved in less straight patterns (Fig 6D), and exhibited a decreased frequency of turning angles near 0 indicative of loss of persistence (Fig EV5A). In keeping with this aberrant migratory behavior, phalloidin staining revealed a higher prevalence of stress fiber type of actin network in *Ovol2* SSKO colonies than in controls, which displayed predominantly cortical type of actin organization (Fig 6E and F). Collectively, these data indicate that Ovol2 is required for directional migration of Bu-HFSCs *ex vivo*.

The upregulation of *Zeb1* expression in the absence of *Ovol2* and a known role for EMT in conferring cell motility [23] led us to ask whether loss of *Zeb1* might normalize the aberrant migratory behavior of *Ovol2*-deficient Bu-HFSCs. To do this, we generated mice containing floxed alleles of both *Ovol2* and *Zeb1* and acutely deleted the two genes, singly or in combination, in Bu-HFSCs using Cre-expressing adenoviruses (Ade-Cre; Fig EV5B–E). Distinct from *Ovol2* SSKO Bu-HFSCs where *Ovol2* deficiency is chronic, acute
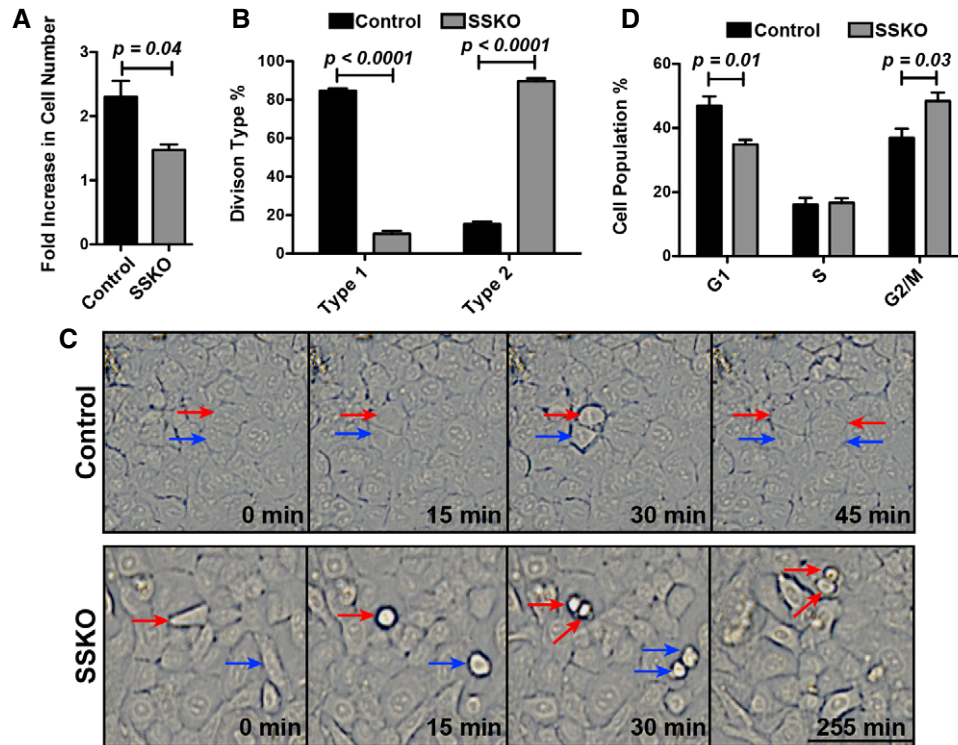
Figure 5. Ovol2-deficient Bu-HFSCs display aberrant cell division behavior and arrest in G2/M->G1 transition.

A   Fold change in cell number per colony in an 18-h period (n = 3 pairs; each biological replicate is an average of three different colonies).

B, C   Live imaging reveals an increased frequency of type-II divisions in SSKO culture, as quantified in (B) (n = 3 pairs; each biological replicate is an average of three different colonies); shown in (C) are representative images from a single experiment. Red and blue arrows in (C) mark two individual cells and their division products during time-lapse.

D   Cell cycle analysis of cultured Bu-HFSCs from control and Ovol2 SSKO mice (n = 3 pairs).

Data information: Scale bar, 100 µm in (C). For statistical analysis in (A), (B), and (D), we used an unpaired two-tailed Student's t-test. Error bars in (A), (B), and (D) represent mean ± SEM.

Ovol2 deletion did not result in any detectable difference in Bu-HFSC expansion (Fig EV5F). Live cell imaging revealed decreased directionality/persistence in the migration of Bu-HFSCs with acute Ovol2 deletion similar to that of Ovol2 SSKO cells, and that this defect was near-completely rescued by the simultaneous deletion of Zeb1 (Figs 6G–I and EV5G). These data provide strong evidence for a key role of the Ovol2-Zeb1 regulatory axis in controlling the migratory behavior of adult Bu-HFSCs.

Discussion

While our previous work describes the importance of Ovol1 and Ovol2 TFs in epidermal morphogenesis [21], the current study highlights Ovol2 as a crucial player in skin epithelial repair and regeneration in adult mice. Most notably, our findings underscore a key role for the Ovol2-Zeb1 EMT-regulatory circuit in modulating the migratory behavior of skin epithelial cells, specifically by restricting migration speed and conferring optimal directionality.

To date, involvement of a classical EMT TF in mammalian cutaneous wound healing has only been shown for Slug (Snai2), the loss of which leads to compromised migration of epidermal cells at the

wound leading edge [9,30]. Very little was known about the molecular mechanisms that keep migrating epidermal cells in check so that they are able to maintain or resume epithelial traits. We now find that Ovol2, likely by virtue of its ability to inhibit the expression of EMT-inducing Zeb1, enables wound epidermal cells to migrate slower but with improved directionality and persistence. Thus, counteracting molecular pathways that normally promote and restrict EMT are both active during epidermal wound healing. Conceivably, EMT-promoting TFs such as Slug and possibly Zeb1 can temporarily and mildly relax epithelial rigidity to initiate and facilitate the migration of epidermal cells around the wound, whereas EMT-inhibitory TFs such as Ovol2 restrict this form of epithelial plasticity to ensure that migration is collective and directional toward the wound center for efficient re-epithelialization to occur.

The molecular regulation of epithelial cell migration during HF regeneration remains an even less charted area. Our data reveal for the first time that EMT-regulatory TFs play critical roles in controlling the migratory behavior of Bu-HFSCs and that HF regeneration is inefficient when such mechanisms go awry. Compared to adult IFE stem cells during normal tissue homeostasis, Bu-HFSCs and their early progenies have to travel much further as they embark on the journey to differentiate into specialized cell
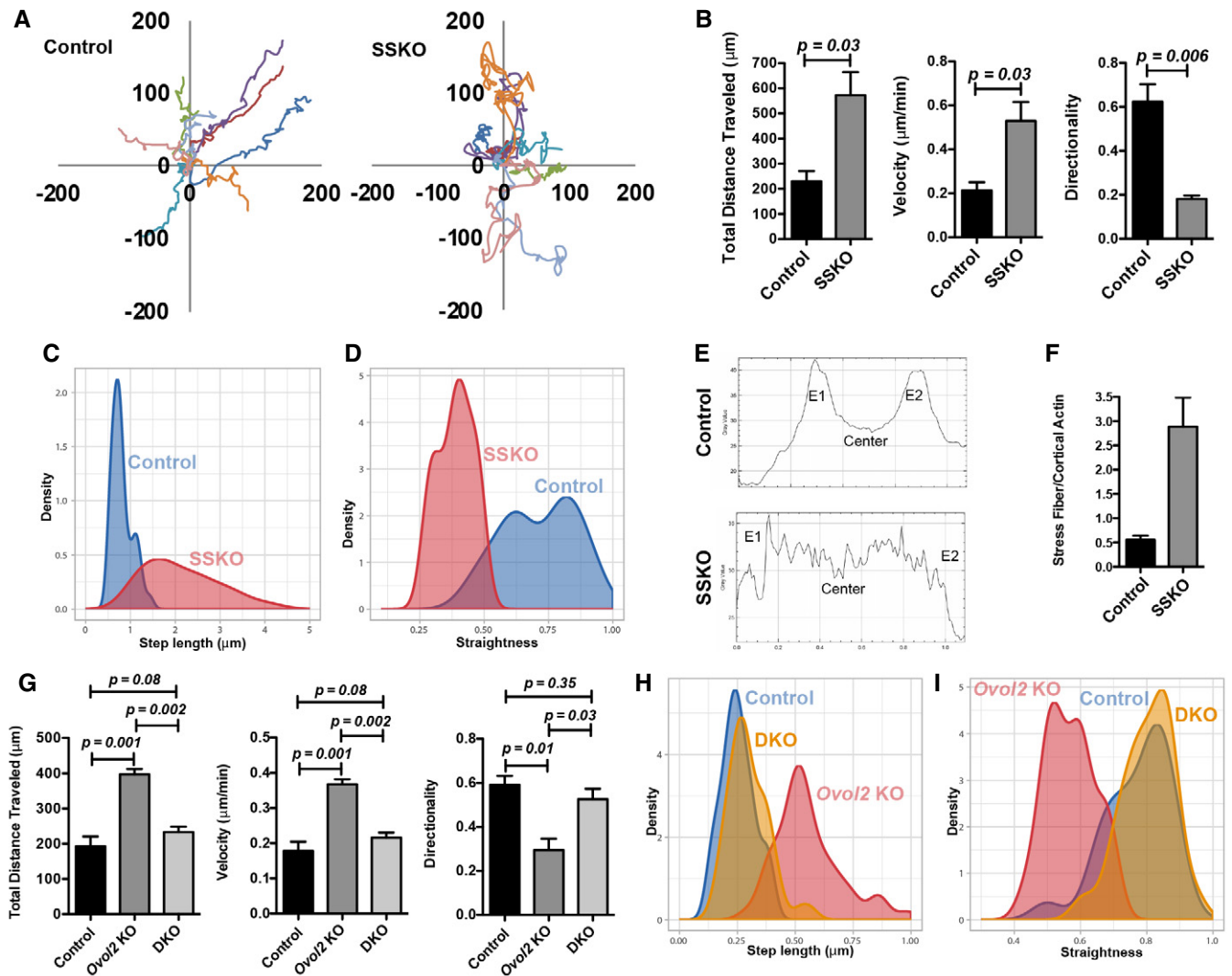
Figure 6. Compromised directional migration of *Ovol2*-deficient Bu-HFSCs is rescued by *Zeb1* deletion.

A   Representative movement tracks of individual cells over an 18-h period.

B–I   (B, G) Quantitative analysis of migration distance, velocity, and directionality of Bu-HFSCs with the indicated genotypes (*n* = 3 pairs; each biological replicate is an average of three different colonies with eight cells tracked per colony). *Ovol2* KO, *Ovol2*-deficient; DKO, *Ovol2*- and *Zeb1*-deficient. (C, H) Step-length comparison among the indicated genotypes. Kolmogorov–Smirnov test: CTL vs. SSKO (C) or *Ovol2* KO (H), $P < 10^{-10}$; CTL vs. DKO (H), $P = 0.06$. (D, I) Straightness distribution comparison among the indicated genotypes. Kolmogorov–Smirnov test: Control vs. SSKO (D) or *Ovol2* KO (I), $P < 10^{-10}$, $P < 10^{-5}$; Control vs. DKO (I), $P = 0.45$. (E) Representative plots that show distribution of fluorescence intensity of actin staining in control and *Ovol2* SSKO Bu-HFSCs. E1 (Edge-1) and E2 (Edge-2) signals correspond to cortical actin near the cell border, whereas center signals correspond to stress fiber actin. (F) Quantification of the ratio between E1 + 2 and center signals (E) in control and *Ovol2* SSKO mice (*n* = 2 pairs).

Data information: For statistical analysis in (B) and (G), we used an unpaired two-tailed Student's *t*-test. Error bars in (B), (F), and (G) represent mean ± SEM.

types during HF regeneration, much like wound margin epidermal cells during re-epithelialization. It is tempting to speculate that epithelial plasticity, specifically partial, reversible EMT-like changes in cell adhesion and cytoskeleton, is an integral part of Bu-HFSC/progeny migration that drives the formation of a new HF. Indeed, as the HF extends downwards, the nuclei of HG cells are more separated from each other than those in the bulge, and they realign as the HG cells reach the epithelial-DP interface [13], implicating dynamic but reversible changes in cell–cell associations. Additional work such as intravital imaging of the *Ovol2*

mutant skin is needed to determine whether and how such dynamic cellular events are affected *in vivo*.

Interestingly, coupled to aberrant cell migration, *Ovol2*-deficient IFE cells, HF matrix cells, and Bu-HFSCs also display significantly reduced proliferation potential. In particular, the aberrant migration and inefficient reattachment of post-mitotic *Ovol2*-deficient Bu-HFSCs along with an inability to transition into the next cell cycle (G2/M->G1) provide correlative evidence for a potential mechanistic link between aberrant migration/adhesion and cell proliferation. However, the lack of a proliferation defect in

Bu-HFSCs following acute *Ovol2* deletion precluded us from using our established assay to ask whether simultaneous deletion of *Zeb1* is able to normalize the cell cycle arrest. Along a similar line, we note that while previous studies identified distinct proliferative and migratory epidermal zones in the healing wound, a recent study found a third epidermal region where migration and proliferation co-exist and where tissue expansion peaks [7]. Intriguingly, here migration regulates the directionality of the cell division plane, providing yet another case of coordinated control of epidermal cell migration and proliferation. Molecular and signaling pathways are known to regulate both migration and proliferation during wound healing [8]. This said, the distinct mode of regulation by Ovol2 vs. known examples such as in the case of BMP signaling [31] is worth noting. It is also important to note that Bu-HFSCs and epidermal cells are two distinct cell types with unique identities and functions; thus, future work is needed to elucidate the potential differences and similarities in mechanism of Ovol2 function in these two cell types in *in vivo* settings.

In *Ovol2* SSKO mice, *K14-Cre*-mediated *Ovol2* deletion occurs during embryogenesis [21]. It is possible that some *Ovol2* deficiency-induced cellular aberrancies take longer time to develop than allowed by the Ade-Cre acute deletion system. A context-dependent notion receives further support from our finding that the migratory and proliferative defects of *Ovol2*-deficient IFE cells and Bu-HFSCs appeared much more pronounced when cells were experiencing non-physiological and/or stressful conditions, such as in culture, upon transplantation, or during wound repair. Perhaps under such conditions, microenvironmental cues such as elevated growth factor concentration and immune cell infiltration cause greater epithelial plasticity, thereby creating a higher demand for molecular mechanisms that maintain epithelial traits such as cell–cell and cell–matrix associations during migration.

Lack of keratinocyte migration is observed in chronic wounds such as those in diabetic patients and is apparently associated with epidermal hyperproliferation [6]. Our animal model studies raise the intriguing possibility that aberrantly increased cell migration at the cost of directionality can be accompanied by epidermal hypoproliferation and together they may underlie some non-healing wounds in human patients. As the current treatment strategies emphasize the promotion of epidermal migration [6], caution should be exercised to create an optimal wound healing tissue microenvironment that enables migration but in a persistent and directional manner.

Materials and Methods

Mice

K14-Cre transgenic mice, floxed (f) and null (−) alleles of *Ovol2*, as well as floxed (f) allele of *Zeb1* have been previously described [32–34]. *ROSA*^mTmG, *ROSA26R*, and *Nu/J* mice are from the Jackson Laboratory (Stock #s 007576, 003474, 002019, respectively). In all mutant analyses, same-sex control littermates were used for comparison. All experiments have been approved and abide by regulatory guidelines of the International Animal Care and Use Committee (IACUC) of the University of California, Irvine.

Morphology and immunostaining

For histological analysis, mouse back skin was shaved, removed, fixed in 4% paraformaldehyde (MP; 150146) in 1× PBS, embedded in paraffin, sectioned, and stained with hematoxylin and eosin (H/E). HF stage identification was based on [35]. For whole-mount analysis, mice were shaved, their skin collected and fat carefully removed, and pigmented HFs were visualized from the dermal side. For indirect immunofluorescence, mouse back skin was freshly frozen in OCT (Fisher; 4585), sectioned at 5–8 μm, and staining was performed using the appropriate antibodies and DAPI (Thermo Fisher; D1306: 1:1,000). The following primary antibodies were used for immunofluorescence: Ovol2 [36]; (rabbit, 1:100), K14 (chicken, 1:1,000; rabbit, 1:1,000; gift of Julie Segre, National Institutes of Health, Bethesda), K15 (Covance, PCK-153P-100, 1:1,000), Ki67 (Cell Signaling, D3B5, 1:1,000), and AE13 (Abcam, ab16113, 1:200). For β-galactosidase histochemistry, mouse back skin wounds were fixed with 0.5% glutaraldehyde (Sigma; G6257), stained overnight at 37°C with X-gal (Denville; CX3000-3), and counterstained with Nuclear Fast Red (VWR; 1B1369). For epidermal sphere analysis in patch assays, injection sites were isolated and fixed in 4% paraformaldehyde, embedded in paraffin, and sectioned. Antigen retrieval was performed by incubating slides in 0.01 M citrate buffer (pH 6.0) in microwave at full power for 3–5 min. For *ROSA*^mTmG analysis, mouse back skin wounds were freshly frozen in OCT, sectioned, and then stained with DAPI. For actin staining of cultured Bu-HFSCs, cells were fixed on plate in 4% paraformaldehyde and subsequently stained for K14 and actin (Phalloidin, Invitrogen A12379, 1:250). Thin section images were taken with an inverted fluorescence microscope (Eclipse E600; Nikon) using the Plan-Fluor 10X DIC L 0.30, Plan-Apo-chromat 20× N.A. 0.75, or Plan-Fluor 40× N.A. 0.75 objectives (Nikon) and a camera (RT Slider; Diagnostic Instruments) equipped with SPOT 4.0.9 software (Diagnostic Instruments). Thick section images were taken at room temperature with the Zeiss LSM700 confocal microscope using EC Plan-Neofluar 10×/0.30 objective. Analysis of Phalloidin staining intensity was done using the Plot Profile tool in Fiji.

Wound healing

Mice were anesthetized using isoflurane (Primal Healthcare; NDC-66794-017-25), backs shaved, and then 4-mm punch (Integra; 33–34) was used to generate a full-thickness wound on each side of the mouse. For re-epithelialization measurements, splints were fastened surrounding the punch. To generate splints, a 5-mm punch biopsy (Integra; 33–35) was used to generate a hole in 1.5-cm-diameter circular piece of silicone (Life; P18178) and then stitched over the wound. Wound diameter was measured every 24 h. For expression analysis, 6-mm punch biopsies (Integra; 33–36) were made, and then, a 12-mm-diameter portion was collected 4 days after wounding. An 8-mm-diameter portion was removed from the center and used as leading edge sample, while the remaining was used as the proliferative zone sample. For *ex vivo* explant assay, mouse back skin was shaved, removed, fat was scrapped away; remaining hair was removed with brief treatment with Nair and then thoroughly rinsed with 1× PBS. A 4-mm punch biopsy was collected as wound explants, which were then placed onto a

well-containing 6 μl Matrigel (BD; 354230) in a 6-well tissue culture dish that was pre-coated with 10 μM fibronectin (EMD Millipore; FC010) for 1 h.

Isolation, culture, and/or infection of NBPKs and Bu-HFSCs

NBPKs were isolated as reported [37] with minor modifications. Briefly, epidermal and dermal separation was achieved with an overnight dispase treatment (Stem Cell Technologies; 07913). Keratinocytes were then isolated from separated epidermis using 0.25% trypsin (Sigma; T4799). Dermal cells were isolated from separated dermis using a 0.25% collagenase (Sigma; C9091) digestion at 37°C for 2 h. For growth curve and clonal assays, freshly isolated NBPKs were cultured on tissue culture plastics without fibroblast feeders in low-Ca^{2+} keratinocyte E-media. For gene expression analysis, NBPKs were cultured on mitotically inactivated J2-3T3 fibroblasts in low-Ca^{2+} keratinocyte E-media. Detailed instructions for J2-3T3 culture and mitotic inactivation can be found in [38]. For growth curve analysis, 10,000 NBPKs were plated per well onto 12-well plates in triplicate. Every 24 h, cells were harvested using 0.1% trypsin and then counted. For clonal growth analysis, NBPKs were plated at a concentration of 1,000 cells/cm^2 onto 6-cm gridded plates. Two weeks later, a 0.5% crystal violet (Sigma; HT90132) solution made in 1:1 water: methanol was added to the plates to fix and stain the cells. Plates were then rinsed with DI water and imaged.

Isolation and subsequent culture of Bu-HFSCs were as reported [38] with minor modifications. Briefly, back skin was cut into ~8 equal pieces and spread dermis side down in 0.25% trypsin and incubated at 37°C for 60 min. Subsequently, epidermis was gently scraped off and then mixed with low-Ca^{2+} keratinocyte E-media, filtered with 70- and 40-μm filters, spun down, and resuspended in low-Ca^{2+} keratinocyte E-media. Adult keratinocytes were stained for CD49f-PE (BD; 555736), CD34-Alexa700 (BD, 560518; clone RAM34), and 7AAD (BD; 559925), followed by sorting using a BD FACSAria™ Fusion Sorter. Adenoviral infection of Bu-HFSCs was based on [39], using Ade-Cre viruses at a multiplicity of infection of 50 (Vector Biolabs; 1772).

Cell cycle analysis

Cell cycle analysis was performed on Bu-HFSCs after 2 weeks of culture. Cells (Bu-HFSCs and feeders) were removed from plate using 0.1% trypsin and then fixed with cold 70% EtOH for 30 min at 4°C. Cells were washed twice in 1× PBS and then stained with CD49f-FITC (BD; 555735) for 30 min at room temperature in the dark. After two washes in 1× PBS, cells were stained with FxCycle™ PI/RNase Staining Solution (Life; F10797) for 15 min and then immediately analyzed using ACEA NovoCyte™ Flow Cytometer.

Patch assay

Patch assay was performed according to published procedures [28,40]. Briefly, total adult epidermal cells (500,000) from 7- to 8-week-old mice were combined with dermal cells (1,000,000) freshly isolated from newborn C57BL/6J mice. The mixture was subcutaneously injected into 7-week-old Nu/J mice, which were examined 2 weeks later.

Live cell imaging

Wound explants and cells were cultured on either 6-cm or 6-well plates and incubated within a microscope chamber at 37°C with 5% CO$_2$. Imaging was performed using the Keyence BZ-X700 microscope for 18-h periods with images taken every 15 min. Images were then exported and analyzed in FIJI using the Manual Tracking plugin. Each initial cell position was set to coordinates of (0,0). Step lengths were calculated for each step for each cell track, and turning angles were calculated based on pairs of cell track segments, i.e., $((x_{t-1}, x_t), (x_t, x_{t+1}))$. The straightness was defined as D_w/L_w where D_w is the total displacement for a given number of steps (window size), and L_w is the total path length in this window. A window size of 70 steps was used.

RNA isolation, quantitative RT–PCR, and RNA-Seq

For RNA isolation, Trizol (Life; 15596018) was used as per manufacturer's instructions. One microgram of RNA was used to generate cDNA (Applied Biosystems; 4368814) as per manufacturer's instructions. qPCR was performed using a Bio-Rad CFX96 Real-Time System and SsoAdvanced Universal SYBR® Green Supermix (Bio-Rad; 172-5271). Primers sequences used for expression analysis are as follows: *Ovol2* F: AGCTTCACGACGCCCAAGGC; *Ovol2* R: GCCG CAGAAGGTGCACAGGT; *Zeb1* F: ACCGCCGTCATTTATCCTGAG; *Zeb1* R: CATCTGGTGTTCCGTTTTCATCA; *Vim* F: GGAGATGCTCCA GAGAGAGG; *Vim* R: ATTCCACTTTCCGTTCAAGG; *Ki67* F: CATCAG CCCATGATTTTGCAAC; *Ki67* R: CTGCGAAGAGAGCATCCATC; *Cdk1* F: TTCCACGGCGACTCAGAGAT; *Cdk1* R: AGCAAATCCAAGCCGTT CTC; *Gapdh* F: CCTGCCAAGTATGATGAC; *Gapdh* R: GGAGTTGCT GTTGAAGTC. For RNA-Seq, optimal-quality RNAs (RNA integrity numbers > 9) were used for cDNA library preparation. Full-length cDNA library amplification was performed as previously described [41,42]. Briefly, 1 ng of total RNA was reverse-transcribed and the resulting cDNA was preamplified for 17 cycles. Tagmentation of cDNA was carried out using the Nextera DNA Sample Preparation Kit (Illumina; FC-121-1031). The Tn6 tagmentation reaction was carried out at 55°C for 5 min and purified using a PCR Purification Kit (Qiagen; 28104). Adapter-ligated fragments were amplified using limited cycle enrichment PCR with Nextera barcodes for seven continuous cycles. The resulting libraries were purified using AMPure XP beads (Beckman Coulter; A63880) and were multiplexed and sequenced as paired end on a HiSeq 2500 Illumina sequencing platform. Sequencing reads were mapped to the mm9 mouse genome using BowTie2 [43], and splice junctions between exons were mapped using Tophat2 [44]. Analysis of differential gene expression was accomplished using CuffDiff [45]. Differentially expressed genes were used for GO analysis. Gene FPKM values were used for downstream analysis that included GSEA [46].

Data availability

Gene expression data are provided in the Excel files and have been deposited to GEO (GSE118915). https://www.ncbi.nlm.nih.gov/geo/query/acc.cgi?acc=GSE118915

Expanded View for this article is available online.

Acknowledgements

Author contributions

XD conceived the study, and DH and XD designed the project and experiments; DH, PS, ALM, XM, and YZ performed the experiments; MVP assisted in patch assay; ALM and QN assisted in cell tracking analysis; MPS, SB, GB, and TB provided animals with a *Zeb1* flox allele; DH and XD interpreted the data; DH, ALM, and XD wrote the manuscript; DH, ALM, MVP, QN, TB, and XD edited the manuscript.

Conflict of interest

The authors declare that they have no conflict of interest.

References

1. Theveneau E, Mayor R (2013) Collective cell migration of epithelial and mesenchymal cells. *Cell Mol Life Sci* 70: 3481−3492

2. Rorth P (2009) Collective cell migration. *Annu Rev Cell Dev Biol* 25: 407−429

3. Friedl P, Gilmour D (2009) Collective cell migration in morphogenesis, regeneration and cancer. *Nat Rev Mol Cell Biol* 10: 445−457

4. Hsu YC, Li L, Fuchs E (2014) Emerging interactions between skin stem cells and their niches. *Nat Med* 20: 847−856

5. Shaw TJ, Martin P (2009) Wound repair at a glance. *J Cell Sci* 122: 3209−3213

6. Eming SA, Martin P, Tomic-Canic M (2014) Wound repair and regeneration: mechanisms, signaling, and translation. *Sci Transl Med* 6: 1−16

7. Park S, Gonzalez DG, Guirao B, Boucher JD, Cockburn K, Marsh ED, Mesa KR, Brown S, Rompolas P, Haberman AM *et al* (2017) Tissue-scale coordination of cellular behavior promotes epidermal wound repair in live mice. *Nat Cell Biol* 19: 155−164

8. Haensel D, Dai X (2018) Epithelial-to-mesenchymal transition in cutaneous wound healing: where we are and where we are heading. *Dev Dyn* 247: 473−480

9. Arnoux V, Come C, Kusewitt DF, Hudson LG, Savagner P (2005) Cutaneous wound reepithelialization: a partial and reversible EMT. In *Rise and fall of epithelial phenotype*. Boston, MA: Springer

10. Schneider MR, Schmidt-Ullrich R, Paus R (2009) The hair follicle as a dynamic miniorgan. *Curr Biol* 19: R132−R142

11. Ito M, Kinzawa K, Hamada K, Cotsarelis G (2004) Hair follicle stem cells in the lower bulge form the secondary germ, a biochemically distinct but functionally equivalent progenitor cell population, at the termination of catagen. *Differentiation* 72: 548−557

12. Greco V, Chen T, Rendl M, Schober M, Pasolli HA, Stokes N, Dela Cruz-Racelis J, Fuchs E (2009) A two-step mechanism for stem cell activation during hair regeneration. *Cell Stem Cell* 4: 155−169

13. Rompolas P, Deschene ER, Zito G, Gonzalez DG, Saotome I, Haberman AM, Greco V (2012) Live imaging of stem cell and progeny behaviour in physiological hair-follicle regeneration. *Nature* 487: 496−499

14. Zhang YV, Cheong J, Ciapurin N, McDermitt DJ, Tumbar T (2009) Distinct self-renewal and differentiation phases in the niche of infrequently dividing hair follicle stem cells. *Cell Stem Cell* 5: 267−278

15. Gonzales KAU, Fuchs E (2017) Skin and its regenerative powers: an alliance between stem cells and their niche. *Dev Cell* 43: 387−401

16. Vagnozzi AN, Reiter JF, Wong SY (2015) Hair follicle and interfollicular epidermal stem cells make varying contributions to wound regeneration. *Cell Cycle* 14: 3408−3417

17. Veniaminova NA, Vagnozzi AN, Kopinke D, Do TT, Murtaugh LC, Maillard I, Dlugosz AA, Reiter JF, Wong SY (2013) Keratin 79 identifies a novel population of migratory epithelial cells that initiates hair canal morphogenesis and regeneration. *Development* 140: 4870−4880

18. Rompolas P, Mesa KR, Greco V (2013) Spatial organization within a niche as a determinant of stem-cell fate. *Nature* 502: 513−518

19. Adam RC, Yang H, Rockowitz S, Larsen SB, Nikolova M, Oristian DS, Polak L, Kadaja M, Asare A, Zheng D *et al* (2015) Pioneer factors govern super-enhancer dynamics in stem cell plasticity and lineage choice. *Nature* 521: 366−370

20. Ge Y, Gomez NC, Adam RC, Nikolova M, Yang H, Verma A, Lu CP, Polak L, Yuan S, Elemento O *et al* (2017) Stem cell lineage infidelity drives wound repair and cancer. *Cell* 169: 636−650 e614

21. Lee B, Villarreal-Ponce A, Fallahi M, Ovadia J, Sun P, Yu QC, Ito S, Sinha S, Nie Q, Dai X (2014) Transcriptional mechanisms link epithelial plasticity to adhesion and differentiation of epidermal progenitor cells. *Dev Cell* 29: 47−58

22. Watanabe K, Villarreal-Ponce A, Sun P, Salmans ML, Fallahi M, Andersen B, Dai X (2014) Mammary morphogenesis and regeneration require the inhibition of EMT at terminal end buds by Ovol2 transcriptional repressor. *Dev Cell* 29: 59−74

23. Nieto MA, Huang RY, Jackson RA, Thiery JP (2016) Emt: 2016. *Cell* 166: 21−45

24. Park SA, Teixeira LB, Raghunathan VK, Covert J, Dubielzig RR, Isseroff RR, Schurr M, Abbott NL, McAnulty J, Murphy CJ (2014) Full-thickness splinted skin wound healing models in db/db and heterozygous mice: implications for wound healing impairment. *Wound Repair Regen* 22: 368−380

25. Aragona M, Dekoninck S, Rulands S, Lenglez S, Mascre G, Simons BD, Blanpain C (2017) Defining stem cell dynamics and migration during wound healing in mouse skin epidermis. *Nat Commun* 8: 14684

26. Keyes BE, Liu S, Asare A, Naik S, Levorse J, Polak L, Lu CP, Nikolova M, Pasolli HA, Fuchs E (2016) Impaired epidermal to dendritic T cell signaling slows wound repair in aged skin. *Cell* 167: 1323−1338 e1314

27. Blanpain C, Lowry WE, Geoghegan A, Polak L, Fuchs E (2004) Self-renewal, multipotency, and the existence of two cell populations within an epithelial stem cell niche. *Cell* 118: 635−648

28. Zheng Y, Du X, Wang W, Boucher M, Parimoo S, Stenn K (2005) Organogenesis from dissociated cells: generation of mature cycling hair follicles from skin-derived cells. *J Invest Dermatol* 124: 867−876

29. Sorce B, Escobedo C, Toyoda Y, Stewart MP, Cattin CJ, Newton R, Banerjee I, Stettler A, Roska B, Eaton S *et al* (2015) Mitotic cells contract actomyosin cortex and generate pressure to round against or escape epithelial confinement. *Nat Commun* 6: 8872

30. Hudson LG, Newkirk KM, Chandler HL, Choi C, Fossey SL, Parent AE, Kusewitt DF (2009) Cutaneous wound reepithelialization is compromised in mice lacking functional Slug (Snai2). *J Dermatol Sci* 56: 19−26

31. Lewis CJ, Mardaryev AN, Poterlowicz K, Sharova TY, Aziz A, Sharpe DT, Botchkareva NV, Sharov AA (2014) Bone morphogenetic protein signaling suppresses wound-induced skin repair by inhibiting keratinocyte proliferation and migration. *J Invest Dermatol* 134: 827−837

32. Andl T, Ahn K, Kairo A, Chu EY, Wine-Lee L, Reddy ST, Croft NJ, Cebra-Thomas JA, Metzger D, Chambon P *et al* (2004) Epithelial Bmpr1a regulates differentiation and proliferation in postnatal hair follicles and is essential for tooth development. *Development* 131: 2257−2268

33. Unezaki S, Horai R, Sudo K, Iwakura Y, Ito S (2007) Ovol2/Movo, a homologue of *Drosophila* ovo, is required for angiogenesis, heart formation and placental development in mice. *Genes Cells* 12: 773–785

34. Brabletz S, Lasierra Losada M, Schmalhofer O, Mitschke J, Krebs A, Brabletz T, Stemmler MP (2017) Generation and characterization of mice for conditional inactivation of Zeb1. *Genesis* 55: e23024

35. Muller-Rover S, Handjiski B, van der Veen C, Eichmuller S, Foitzik K, McKay I, Stenn K, Paus R (2001) A comprehensive guide for the accurate classification of murine hair follicles in distinct hair cycle stages. *J Invest Dermatol* 117: 3–15

36. Mackay DR, Hu M, Li B, Rheaume C, Dai X (2006) The mouse Ovol2 gene is required for cranial neural tube development. *Dev Biol* 291: 38–52

37. Lichti U, Anders J, Yuspa SH (2008) Isolation and short-term culture of primary keratinocytes, hair follicle populations and dermal cells from newborn mice and keratinocytes from adult mice for *in vitro* analysis and for grafting to immunodeficient mice. *Nat Protoc* 3: 799–810

38. Nowak JA, Fuchs E (2009) Isolation and culture of epithelial stem cells. *Methods Mol Biol* 482: 215–232

39. Haensel D, McNeil MA, Dai X (2018) *Ex vivo* imaging and genetic manipulation of mouse hair follicle bulge stem cells. In *Methods in Molecular Biology*. New York City, NY: Humana Press

40. Zheng Y, Hsieh JC, Escandon J, Cotsarelis G (2016) Isolation of mouse hair follicle bulge stem cells and their functional analysis in a reconstitution assay. *Methods Mol Biol* 1453: 57–69

41. Picelli S, Bjorklund AK, Faridani OR, Sagasser S, Winberg G, Sandberg R (2013) Smart-seq2 for sensitive full-length transcriptome profiling in single cells. *Nat Methods* 10: 1096–1098

42. Picelli S, Bjorklund AK, Reinius B, Sagasser S, Winberg G, Sandberg R (2014) Tn5 transposase and tagmentation procedures for massively scaled sequencing projects. *Genome Res* 24: 2033–2040

43. Langmead B, Salzberg SL (2012) Fast gapped-read alignment with Bowtie 2. *Nat Methods* 9: 357–359

44. Kim DPG, Trapnell C, Pimentel H, Kelley R, Salzberg SL (2013) TopHat2: accurate alignment of transcriptomes in the presence of insertions, deletions and gene fusions. *Genome Biol* 14: R36

45. Trapnell CHD, Sauvageau M, Goff L, Rinn J, Pachter L (2012) Differential analysis of gene regulation at transcript resolution with RNA-seq. *Nat Biotechnol* 31: 46–53

46. Subramanian A, Tamayo P, Mootha VK, Mukherjee S, Ebert BL, Gillette MA, Paulovich A, Pomeroy SL, Golub TR, Lander ES *et al* (2005) Gene set enrichment analysis: a knowledge-based approach for interpreting genome-wide expression profiles. *Proc Natl Acad Sci USA* 102: 15545–15550